NASA Technical Memorandum 110396 USAATCOM Technical Report 96-A-011

Aerodynamic Limitations of the UH-60A Rotor

Colin P. Coleman and William G. Bousman

August 1996

National Aeronautics and
Space Administration

US Army
Aviation and Troop Command

NASA Technical Memorandum 110396 USAATCOM Technical Report 96-A-011

Aerodynamic Limitations of the UH-60A Rotor

Colin P. Coleman, *Ames Research Center, Moffett Field, California*
William G. Bousman, *Aeroflightdynamics Directorate, U.S. Army Aviation and Troop Command, Ames Research Center, Moffett Field, California*

August 1996

National Aeronautics and
Space Administration

Ames Research Center
Moffett Field, CA 94035-1000

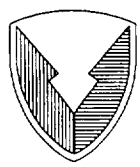

US Army
Aviation and Troop Command

Aeroflightdynamics Directorate
Moffett Field, CA 94035-1000

Aerodynamic Limitations of the UH-60A Rotor

COLIN P. COLEMAN AND WILLIAM G. BOUSMAN*

Ames Research Center

Summary

High quality airloads data have been obtained on an instrumented UH-60A in flight and these data provide insight into the aerodynamic limiting behavior of the rotor. At moderate weight coefficients and high advance ratio limiting performance is largely caused by high drag near the blade tip on the advancing side of the rotor as supercritical flow develops on the rotor with moderate to strong shocks on both surfaces of the blade. Drag divergence data from two-dimensional airfoil tests show good agreement with the development of the supercritical flow regions. Large aerodynamic pitching moments are observed at high advance ratio, as well, and these pitching moments are the source of high torsional moments on the blade and control system loads. These loads occur on the advancing side of the disk and are not related to blade stall which does not occur for these weight coefficients. At high weight coefficients aerodynamic and structural limits are related to dynamic stall cycles that begin on the retreating side of the blade and, for the most severe conditions, carry around to the advancing side of the blade at the presumed first frequency of the blade/control system.

Introduction

The thrust and power of a helicopter rotor are limited by a number of nonlinear aerodynamic phenomena at the edges of the rotor envelope, but these phenomena are poorly quantified. McHugh (ref. 1) reported on wind tunnel tests of an articulated rotor that was designed with sufficient structural strength that the limiting performance of the rotor was aerodynamic and not structural.

Conventional wisdom holds that the effect of stall on control system fatigue loads, rather than flying quality deterioration, is usually the limiting criterion in establishing the rotor limit. Despite this, there are few published demonstrations of the importance of blade stall for limiting conditions. Ward, in reference 2, as an example, demonstrated that the limiting load condition at low advance ratio on the CH-34 was a result of the vortex wake spacing exciting the second torsion mode rather than blade stall per se. At high speed, comparisons of experimental measurements and calculations (ref. 3) suggest that limit loads are caused by unsteady, three-dimensional flow at the blade tip, and these limitations are not related to blade stall. However, over a considerable portion of the flight envelope it is expected that dynamic stall of the airfoil will be the dominant cause of the limiting loads (refs. 1, 4, and 5).

It is not possible with a conventional rotor to explore McHugh's rotor lift limit because of rotor structural limitations. However, it is possible to approach this boundary and, with adequate rotor instrumentation, to characterize the phenomena that are involved. A UH-60A with a highly instrumented rotor flown in September and October 1993 provided detailed information about the blade surface pressures and structural response. This paper examines these aerodynamic measurements, with a particular emphasis on limiting phenomena that occur on the advancing side of the rotor at moderate thrust coefficients and on the retreating side of the rotor at high thrust coefficients.

The UH-60 Airloads Project team are acknowledged for their persistence in obtaining this data.

Nomenclature

a	speed of sound, ft/sec
b	number of blades
c	blade chord, ft
$\frac{C_{FM}}{\sigma} = \frac{M_F}{\rho bc\Omega^2 R^4}$	flap bending moment (nondimensional)
$\frac{C_{PL}}{\sigma} = \frac{P}{\rho bc\Omega^2 R^3}$	pitch-link force (nondimensional)

*Aeroflightdynamics Directorate, U.S. Army Aviation and Troop Command.

$\frac{C_Q}{\sigma} = \frac{Q}{\rho bc\Omega^2 R^4}$ rotor torque coefficient

$\frac{C_{TM}}{\sigma} = \frac{M_T}{\rho bc\Omega^2 R^4}$ torsion moment (nondimensional)

$\frac{C_w}{\sigma} = \frac{W}{\rho bc\Omega^2 R^3}$ rotor weight coefficient

L section lift, lb/in.

M local Mach number, or pitching moment, in.-lb/in.

$M^2 C_L = \frac{2L}{\rho a^2 c}$ normal force (nondimensional)

$M^2 C_M = \frac{2M}{\rho a^2 c^2}$ normalized pitching moment

$M^2 C_{pl} = \frac{2(p_l - p_\infty)}{\rho a^2}$ normalized pressure coefficient (lower surface)

$M^2 C_{pu} = \frac{2(p_u - p_\infty)}{\rho a^2}$ normalized pressure coefficient (upper surface)

M_F flap bending moment, in.-lb

M_T torsion moment, in.-lb

P pitch-link force, lb

p pressure, lb/in.^{2}

Q main rotor torque, in.-lb

R blade radius, ft

W weight, lb

μ advance ratio

ρ air density, slugs/ft^3

σ rotor solidity

Ω rotor speed, rpm

Flight Test Data

The standard UH-60A was modified to incorporate an extensive instrumentation suite (ref. 6). One blade had a total of 242 pressure transducers which were mounted at various radial and chord stations on both surfaces, and are outlined in figure 1. A second blade was instrumented with strain gauges and accelerometers. Pressure data were sampled at 2142 Hz which corresponds to 500 samples/revolution. Anti-aliasing filters were set at 500 Hz which corresponds to approximately 120 samples/revolution, or an azimuth step size of 1.4 degrees. Approximately five seconds of data were obtained at each level flight test point.

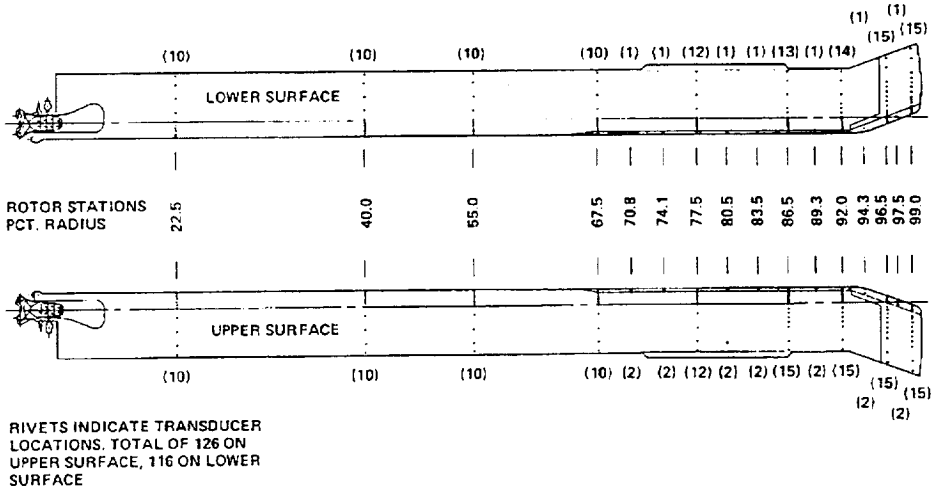

Figure 1. UH-60A instrumented blade showing locations of pressure transducers.

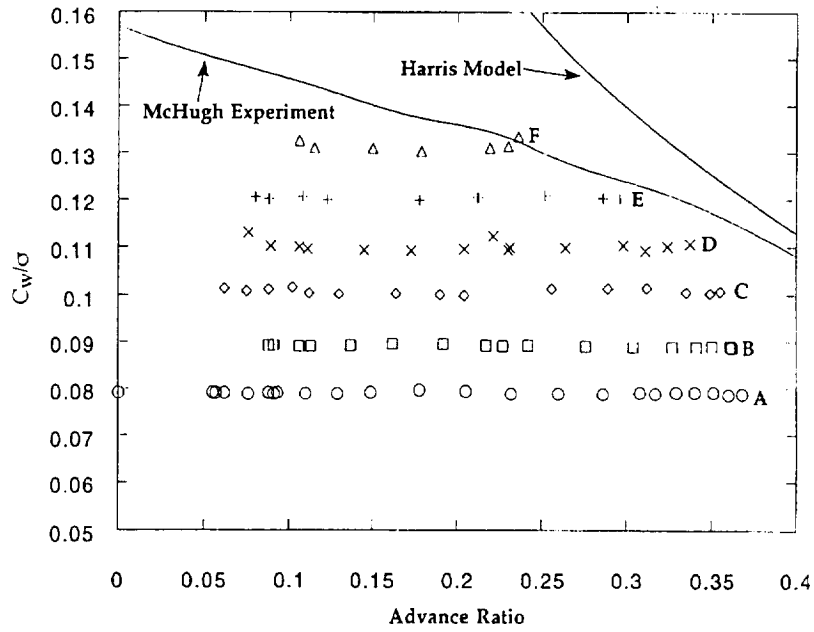

Figure 2. UH-60A level flight data compared to McHugh (ref. 1) and Harris (ref. 7) boundaries.

Figure 2 shows the test points that were flown to investigate the aerodynamic limits of the UH-60A rotor. Advance ratio sweeps were performed at constant C_W/σ within the helicopter's power-limit boundary. Thus, the first and last points for each advance ratio sweep occur at the engine's 30-minute power rating. Also shown on figure 2 are approximate aerodynamic limits based on McHugh's experiment (ref. 1) and a roll-moment balance equation of Harris (ref. 7). The experimental limit is for a propulsive force coefficient of 0.05 and was defined by a reversal in thrust coefficient with increasing collective pitch. The Harris limit is based on a $C_{Lmax} = 1.75$ of the SC1094R8 section (ref. 8) and ignores tip path plane tilt.

The basic behavior of the rotor airloading is shown in figure 3 for three airspeeds at a weight coefficient of 0.08. The plots show the measured section normal force and pitching moment as functions of azimuth and radial station in the manner of Hooper (ref. 9). At an advance ratio of 0.153, the loading that is induced by the vortices of the preceding blades is evident on both the advancing and retreating sides of the disk. This loading causes a down-up pulse as it moves radially inward on the blade on the advancing side and then a up-down pulse on the retreating side as it moves back out toward the blade tip. At higher advance ratios, the effects of vorticity in the wake on the blades is reduced but still evident. As airspeed increases the distribution of the section lift is dominated more and more by a reduction in lift near the blade tip in the second quadrant to accommodate roll-moment balance and to minimize drag due to compressibility. Also seen is the negative lift on the inboard sections of the retreating blade due to reverse flow. This can also be seen in the associated section moment diagram as a strong positive (nose-up) moment near the blade root. The plots of section pitching moment also show the large pitching moments that develop near the blade tip. These pitching moments, which dominate the torsion moments and control system loads are believed to be a consequence of unsteady, three-dimensional flows at the blade tip (ref. 3). The effect of blade sweep has only a minor effect upon these loads.

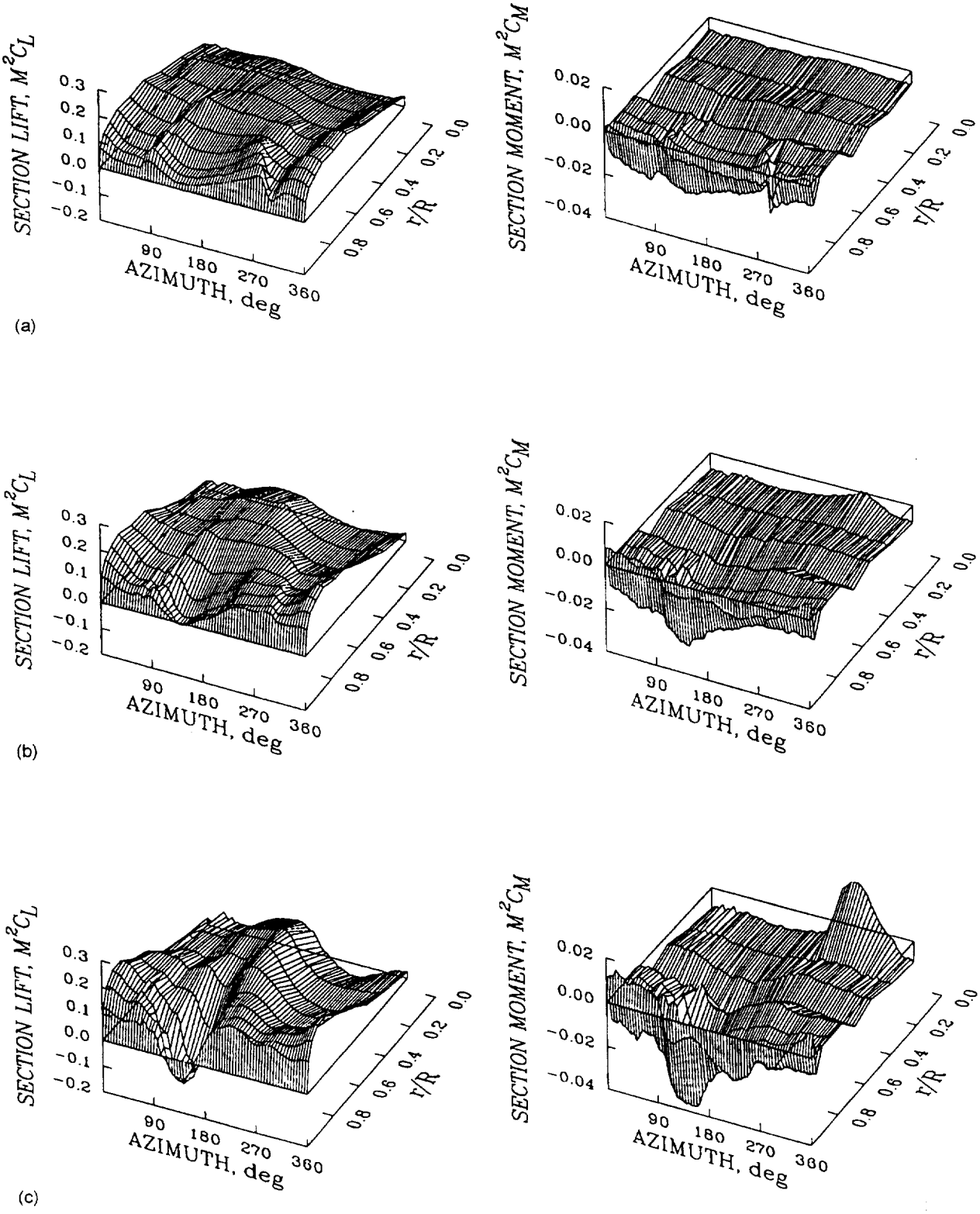

Figure 3. Normalized section lift and pitching moments for three airspeeds; $C_W/\sigma = 0.08$. (a) $\mu = 0.15$, (b) $\mu = 0.26$, (c) $\mu = 0.37$.

The rapid increase of main rotor torque with advance ratio is shown in figure 4. The loading is seen to grow rapidly beyond $\mu = 0.3$. This increase in loading with advance ratio is also reflected in the rise of structural torsion moment and the oscillatory (1/2 peak-to-peak) pitch-link loads. However, structural chordwise bending only increases by roughly 40% of its minimum power value. The characteristics of the pitch-link load measurements are shown in figure 5 as a function of advance ratio and azimuth. The oscillatory behavior of the loads at high advance ratio in the third and fourth quadrants appears at 4/rev. This response is induced by the positive-negative loading on the advancing side of the disk. At $\mu = 0.37$, the pitch-link loads are roughly 280% of the loads experienced at $\mu = 0.15$.

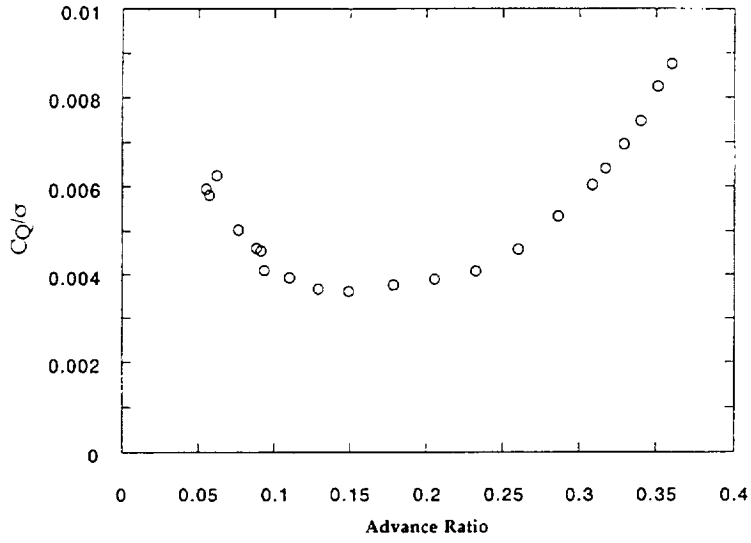

Figure 4. Torque coefficient as a function of advance ratio; $C_W/\sigma = 0.08$.

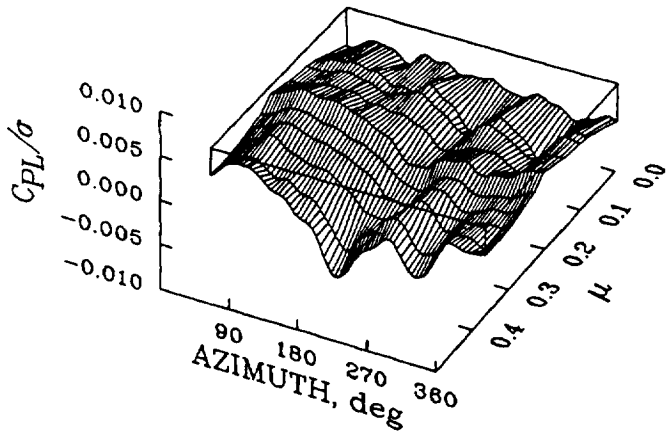

Figure 5. Pitch-link load as a function of blade azimuth and advance ratio; $C_W/\sigma = 0.08$.

Advancing Blade Aerodynamics

Consider the high speed point ($\mu = 0.37$) at $C_W/\sigma = 0.08$, marked as point 'A' in figure 2. This point represents the maximum forward speed power limit of the UH-60A. As advance ratio increases, a pocket of supercritical flow develops on both surfaces of the advancing blade, and this pocket increases in size over the blade up to the power limit. This is shown in figure 6, where the upper and lower pressures at 0.865R, 0.203c are plotted as a function of azimuth and advance ratio. The supercritical flow is readily visible in these figures and the azimuthal points where the divergence Mach number is exceeded are added as solid circles (ref. 8). It is quite reassuring that two-dimensional airfoil data predicts the onset of wave drag so precisely. The pressure distribution of the entire 0.865 section at $\mu = 0.37$ in shown in figure 7 as a function of azimuth. The regions of supercritical flow are clearly seen on both upper and lower surfaces. The most severe area of supercritical flow was found to occur at the 0.965R station, as shown in figure 8. Notice the extent of the supercritical flow in the chordwise direction (up to 0.4c), and the azimuthal extent (50 degrees). Figure 8 also demonstrates the resolution of the data acquisition system, with the area of supercritical flow being sharply defined.

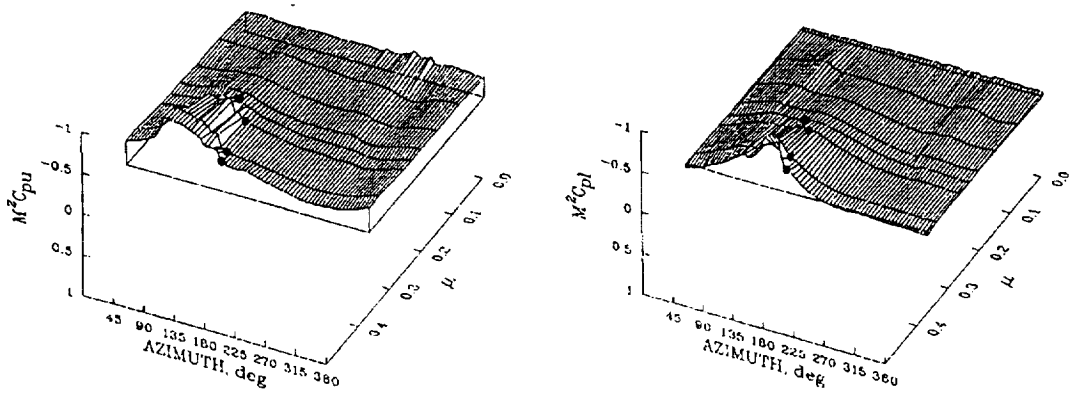

Figure 6. Upper and lower surface normalized pressure coefficients as a function of blade azimuth and advance ratio at 0.865R, 0.203c; $C_W/\sigma = 0.08$. Azimuth for Mach number divergence from 2-D data shown as solid circles.

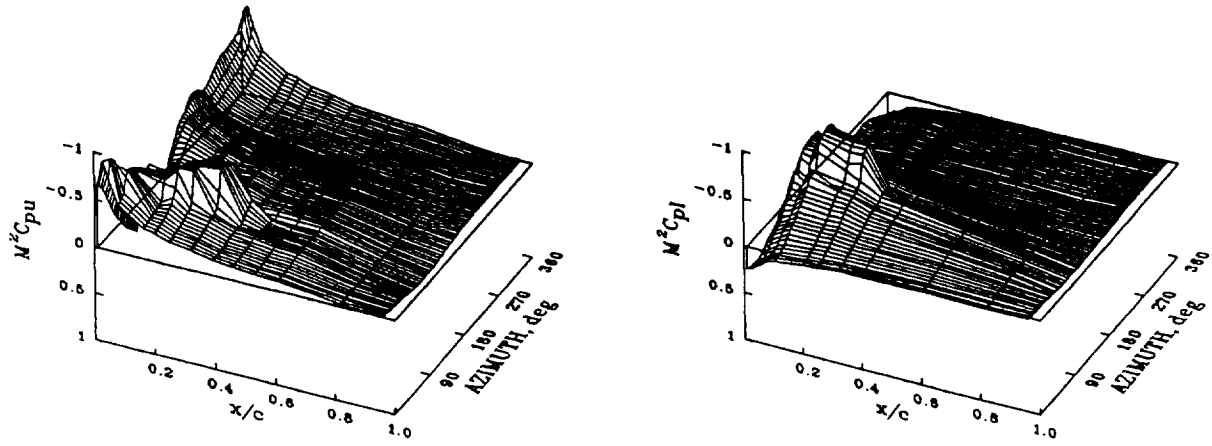

Figure 7. Normalized pressure coefficient as a function of blade chord and azimuth at 0.865R for moderate weight coefficient/high speed case; $C_W/\sigma = 0.08$, $\mu = 0.37$ (Point A).

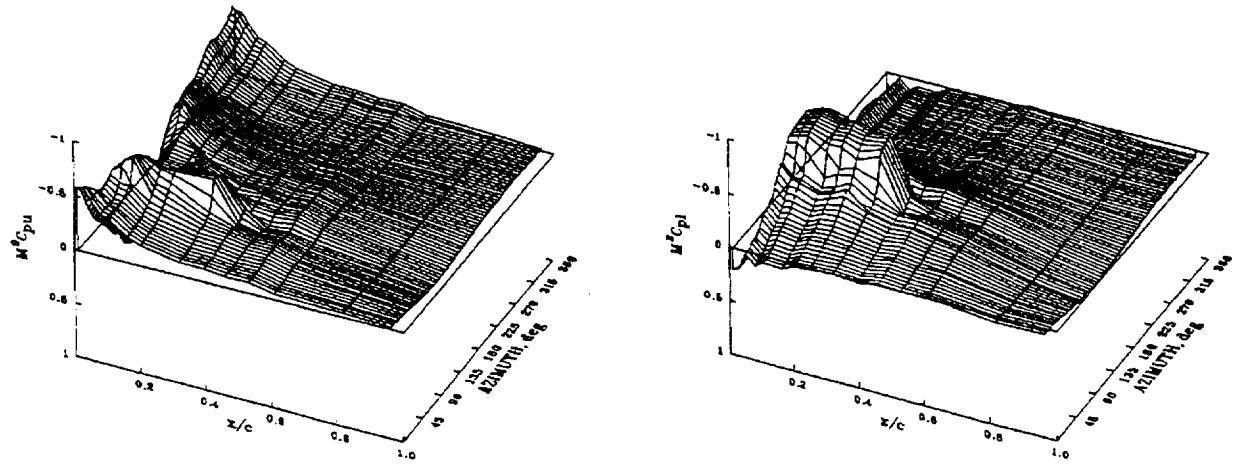

Figure 8. Normalized pressure coefficient as a function of blade chord and azimuth at 0.965R for moderate weight coefficient/high speed case; $C_W/\sigma = 0.08$, $\mu = 0.37$ (Point A).

To show the steadiness of the data with azimuth at $\mu = 0.37$, the lower surface pressure at 0.92R, 0.107c was plotted versus azimuth and cycle (one cycle being equal to one rotor revolution), and is shown in figure 9. The first thing that strikes one is that the data is extremely steady with cycle count, and this is typical of most pressure data obtained. The second interesting point is the appearance of what is believed a shock wave-boundary layer interaction just before the shock passes over the transducer location. This phenomena is shown to occur at exactly the same azimuthal position with each cycle.

The aerodynamic section moment in the region of the blade tip dominates torsion loading in high speed flight, as shown in figure 10. Both the aerodynamic section moment at the blade tip and the pitch-link loads are characterized by large positive (nose-up) moments in the first quadrant with rapid reversal of load so that the moment is negative in the second quadrant. The behavior of the torsional moment and pitch-links are typical of articulated rotors in high speed flight (ref. 10).

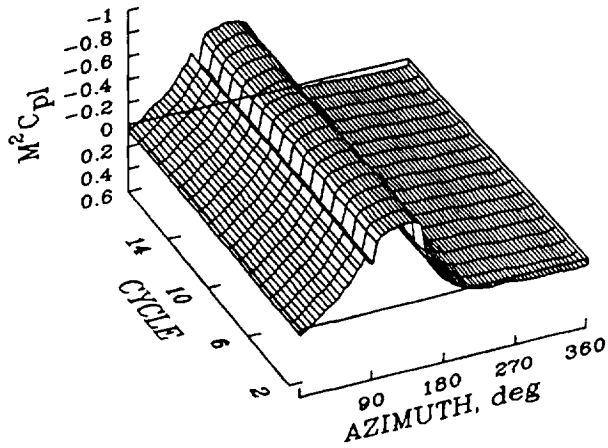

Figure 9. Normalized surface pressure coefficient at 0.107c and 0.92R as a function of azimuth and cycle count for moderate weight coefficient/high speed case; $C_W/\sigma = 0.08$, $\mu = 0.37$ (Point A).

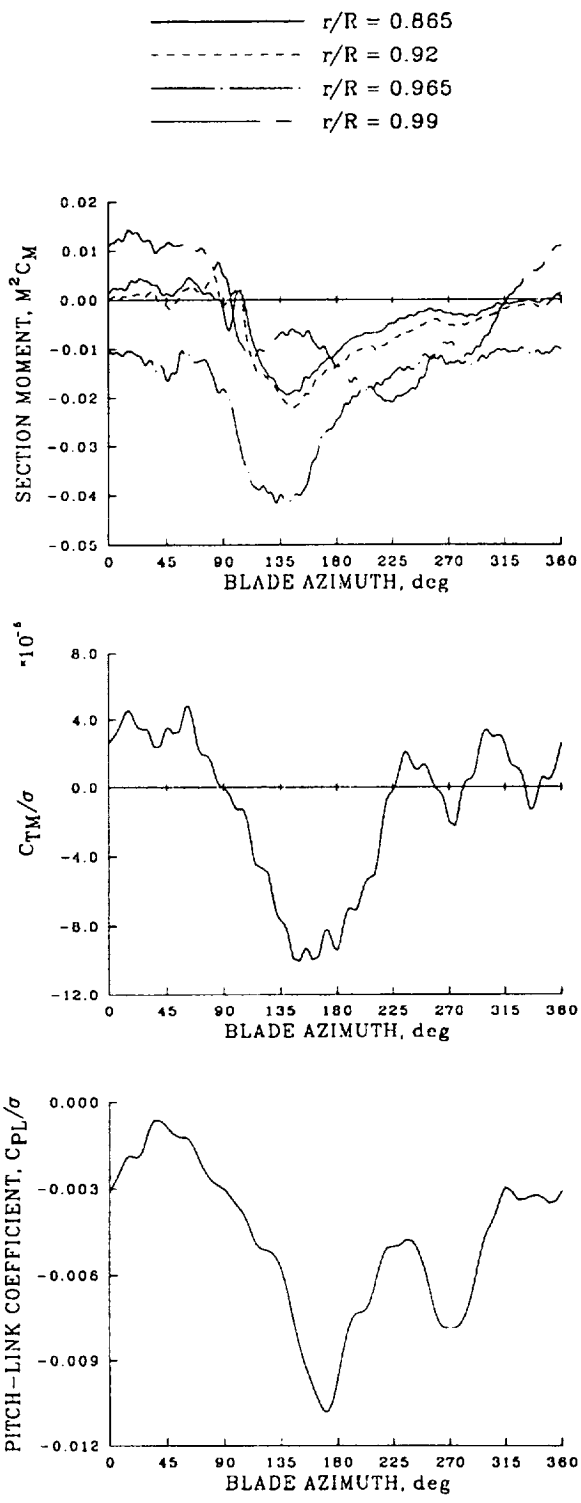

Figure 10. Comparison of normalized section moment on outer portion of blade with torsion moment at 0.30R and pitch-link load for moderate weight coefficient/high speed case; $C_W/\sigma = 0.08$, $\mu = 0.37$ (Point A).

Retreating Blade Aerodynamics

There is no indication of blade stall anywhere on the blade for the high-speed point at $C_W/\sigma = 0.08$. The weight coefficient was increased in steps of 0.01 to examine the development of stall on the rotor; see points A–F in figure 2. Figure 11 shows the section lift and pitching moment at 0.865R as the weight coefficient is increased. The section lift has the same trend with azimuth for lower values of blade loading, exhibiting mainly the decrease in lift on the advancing blade due to compressibility. At $C_W/\sigma = 0.12$, a slight variance of the lift is seen on the retreating side, which is more pronounced at the highest loading of $C_W/\sigma = 0.13$. Here, the lift is seen to decrease and increase rapidly, signaling dynamic stall. This behavior is confirmed by examining the section moment where a small section of stall is noted at $C_W/\sigma = 0.11$, this becomes larger at 0.12, and for $C_W/\sigma = 0.13$ multiple stall cycles are observed.

The stall behavior is examined in figure 12 on a local lift and pitching moment basis. This shows the seven-times increase in pitching moment at the higher blade loading due to the dynamic blade stall behavior. Figure 12 also shows the growth in the stall pocket with increasing blade loading. The associated pitch-link loads are shown in figure 13. At lower values of weight coefficient the pitch-link loads are dominated by a positive to negative load reversal on the advancing side while on the retreating side smaller oscillations are seen at 4/rev. As stall begins to develop the character of the pitch-link load changes with the highest positive load still in the first quadrant, but the most negative load occurs in the third or fourth quadrant and the predominant frequency is now 5.3/rev.

The section pitching moment, torsion moments, and pitch-link loads are compared in figure 14 for $C_W/\sigma = 0.13$. It appears that the two dynamic stall cycles seen here (at 5.3/rev) are the primary cause of the change in the pitch-link behavior.

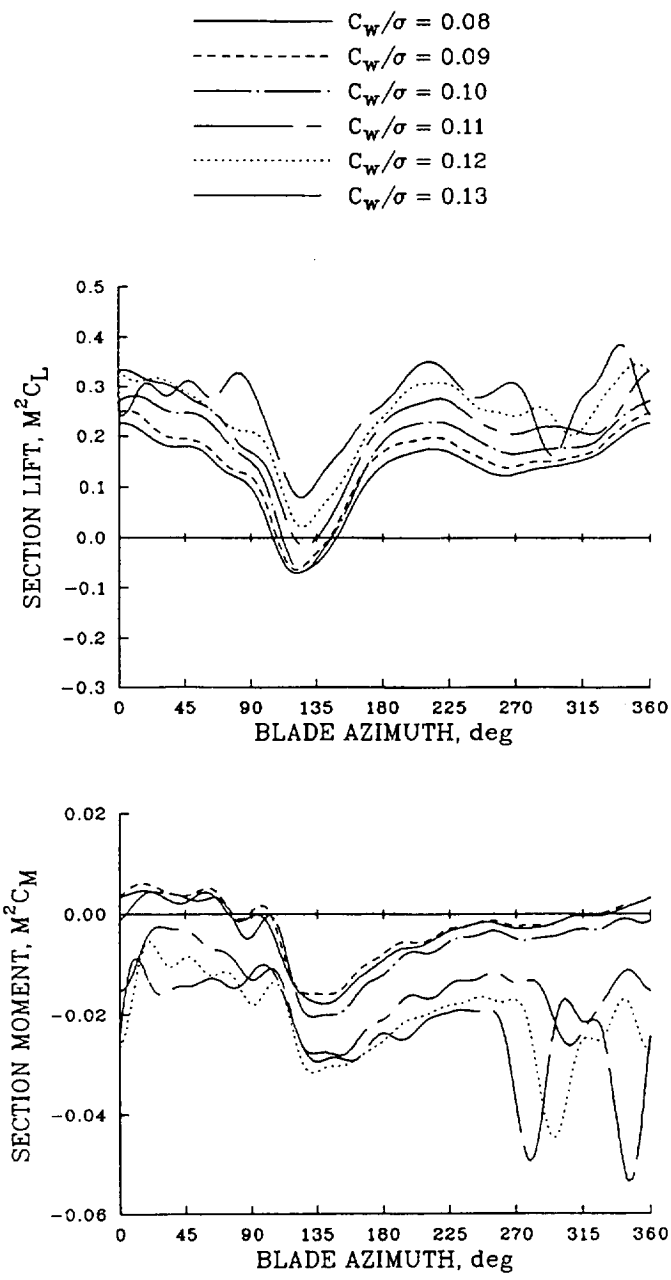

Figure 11. Blade section lift and pitching moment normalized coefficients at 0.865R with increasing weight coefficient at power-limit speeds.

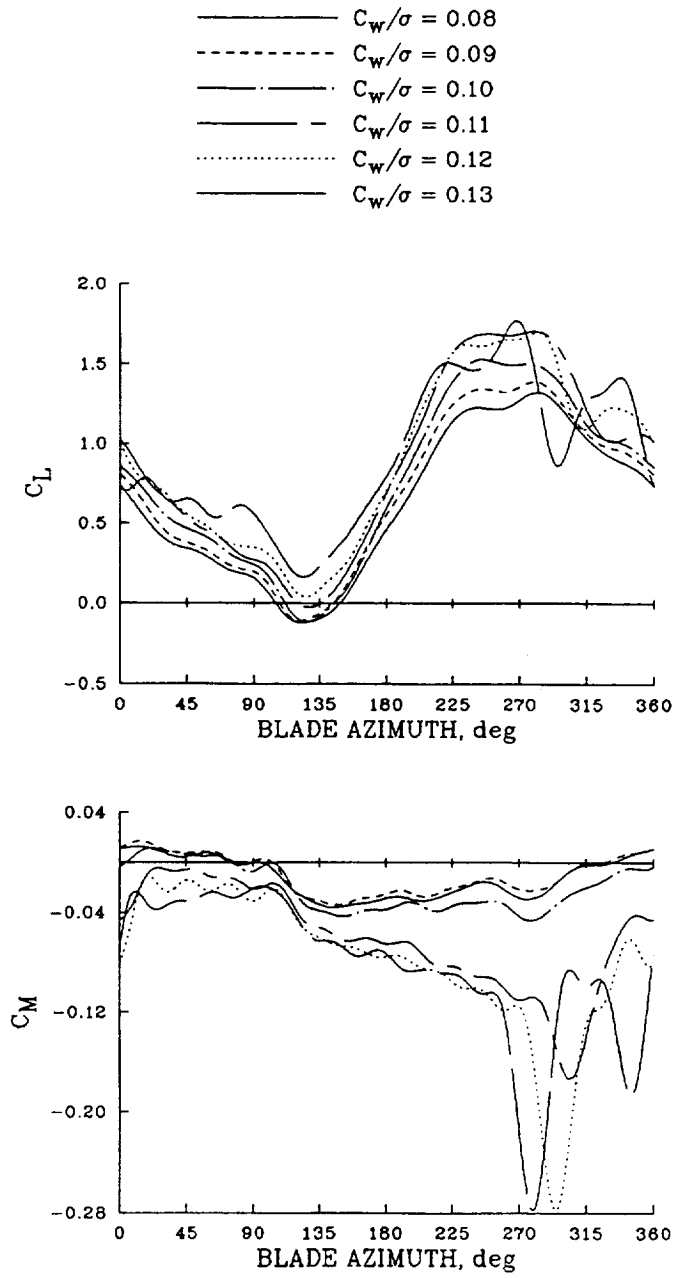

Figure 12. Blade section lift and pitching moment coefficients at 0.865R with increasing weight coefficient at power-limit speeds.

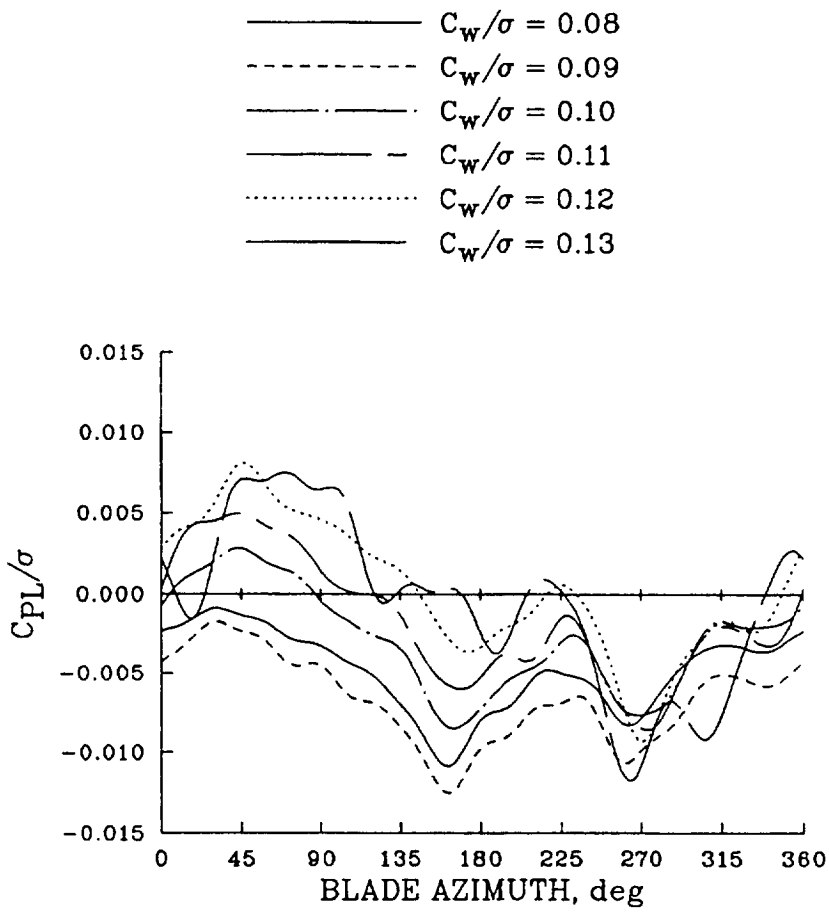

Figure 13. Pitch-link load development with increasing weight coefficient at power-limit speeds.

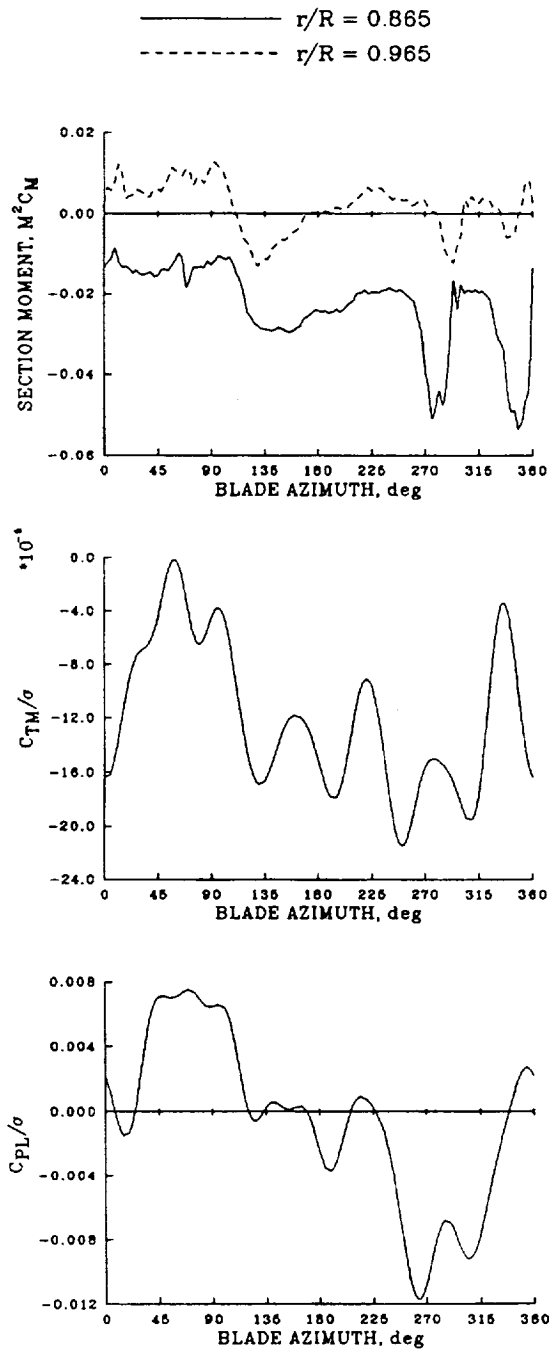

Figure 14. Comparison of section pitching moment, blade torsion moment at 0.30R, and blade pitch-link load for high weight coefficient/high speed case; $C_W/\sigma = 0.13$, $\mu = 0.24$ (Point F).

The upper and lower pressures (Point F) for 0.865R are shown in figure 15 as a function of chordwise station and azimuth. Compressibility effects are still apparent, but now appear on the upper surface (compared to point A, where they were on both surfaces). Deep stall is seen by a vortex (suction peak) moving rearwards over the airfoil from $\psi = 260°$, resulting in stall at the trailing edge at $\psi = 285°$. A second vortex is seen around $\psi = 320°$. Figure 16 once again shows the repeatability of the data over a number of cycles. The 'smoothness' of the data on the advancing side is in contrast to the retreating side, where the unsteady nature of the lift, induced by dynamic stall, carries around to the advancing side to about $\psi = 70°$.

The behavior of the rotor airloading at point F is shown in figure 17. It is interesting to compare this figure with the corresponding behavior at point A in figure 3. The positive-negative loading on the advancing side is reduced, and a reverse flow region is no longer evident by examining the pitching moment behavior. The dynamic stall cycles are very apparent on the retreating side, and these are reflected in the large negative pitching moments.

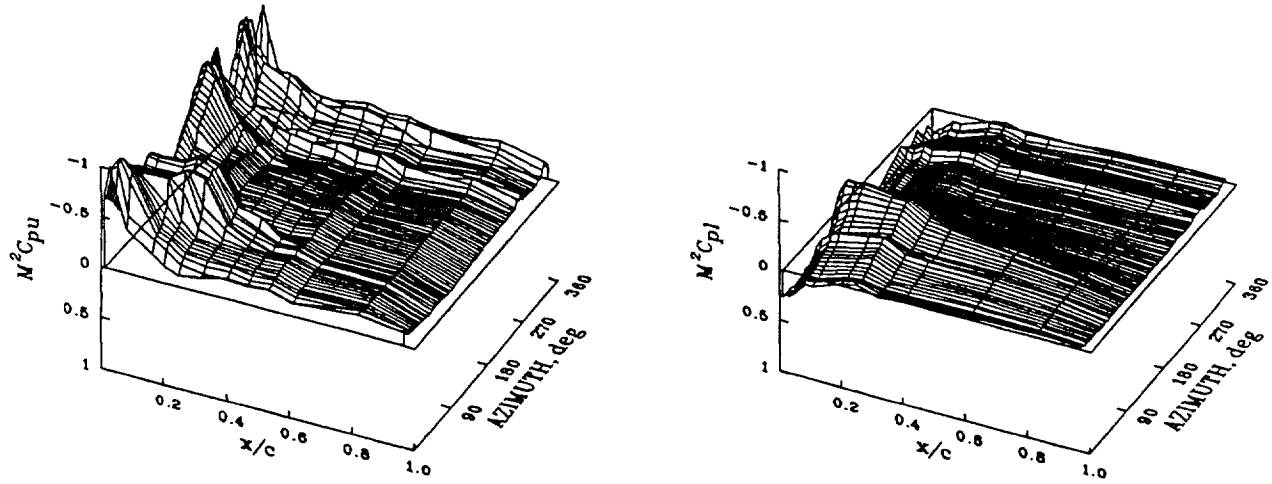

Figure 15. Normalized pressure coefficient as a function of blade chord and azimuth at 0.865R for high weight coefficient/high speed case; $C_W/\sigma = 0.13$, $\mu = 0.24$ (Point F).

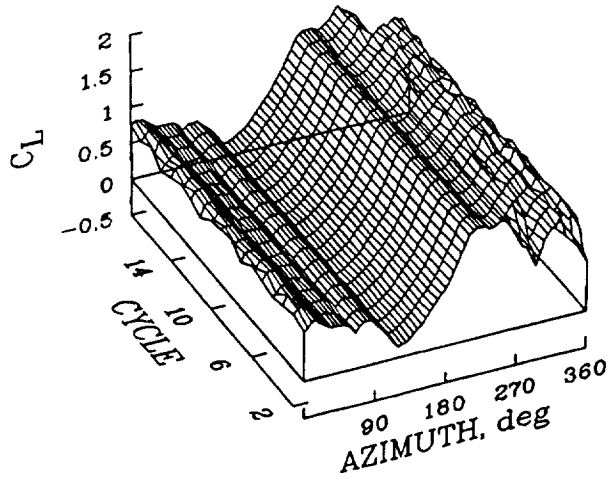

Figure 16. Section lift coefficient at 0.865R as a function of azimuth and cycle count for high weight coefficient/high speed case; $C_W/\sigma = 0.13$, $\mu = 0.24$ (Point F).

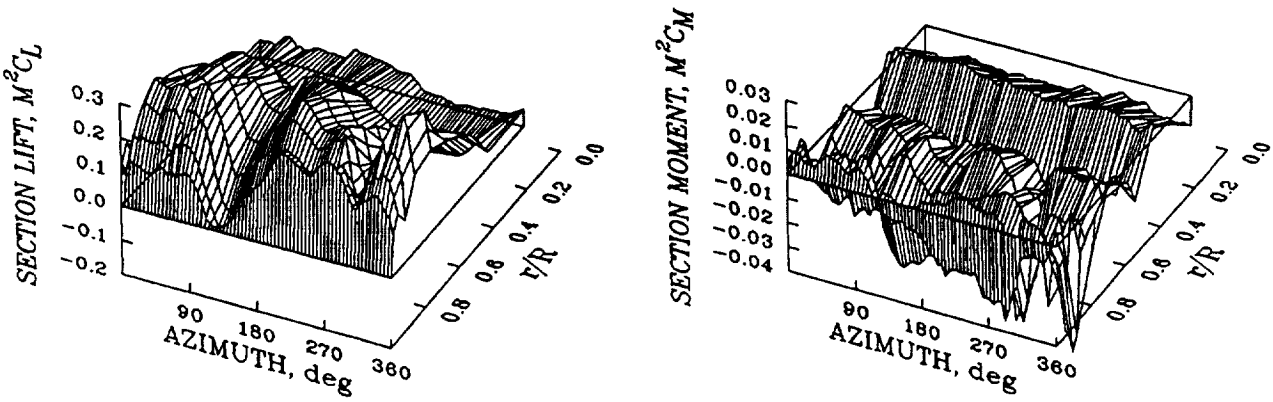

Figure 17. Section lift and pitching moment for high weight coefficient/high speed case; $C_W/\sigma = 0.13$; $\mu = 0.24$ (Point F).

Concluding Remarks

Measured airloads and structural loads obtained on an instrumented UH-60A have been examined for limiting flight conditions. At moderate weight coefficients and at high advance ratio large areas of supercritical flow and moderate to strong shocks are seen on both surfaces of the airfoil on the advancing side of the disk. Comparisons with two-dimensional airfoil data show that these supercritical flow regions are associated with drag divergence on the airfoil and that this increase in profile drag is a significant part of the aircraft power limitations. In addition, the blade pitch-link loads show a rapid increase near the power-limit boundary and it appears that this is largely caused by unsteady, three-dimensional loading on the advancing side of the disk.

Stall develops on the rotor at high values of weight coefficient. Stall is initially seen as a single cycle on the retreating side of the rotor but, as weight coefficient is increased, multiple stall cycles are seen. The characteristic dynamic stall behavior of a shed leading edge vortex is qualitatively seen in the data.

The overall quality of the UH-60A measurements appears good. Comparisons between cycles over a five second record show that the data are quite steady. Even in the presence of dynamic stall the data are shown to be steady while the flow is attached. In addition, the various measurements show good qualitative agreement with each other and it is expected that these data will provide a valuable resource in the development of improved analytical tools.

References

1. McHugh, F.: What Are the Lift and Propulsive Force Limits at High Speed for the Conventional Rotor. American Helicopter Society 34th Annual Forum, May 1978.

2. Ward, J.: Helicopter Rotor Differential Pressures and Structural Response Measured in Transient and Steady-State Maneuvers. Journal of the American Helicopter Society, vol. 16, no. 1, Jan. 1971.

3. Maier, T.; and Bousman, W.: An Examination of the Aerodynamic Moment on Rotor Blade Tips Using Flight Test Data and Analysis. Eighteenth European Rotorcraft Forum, Sept. 1992.

4. Tarzanin, F., Jr.: Prediction of Control Loads Due to Blade Stall. Journal of the American Helicopter Society, vol. 17, no. 2, April 1972.

5. Issacs, N.; and Harrison, R.: Identification of Retreating Blade Stall Mechanisms Using Flight Test Pressure Measurements. American Helicopter Society 45th Annual Forum, May 1989.

6. Kufeld, R.; and Loschke, P.: UH-60 Airloads Program: Status and Plans. AIAA Aircraft Design Systems and Operations Meeting, Sept. 1991.

7. Harris, F.: Rotary Wing Aerodynamics—Historical Perspective and Important Issues. National Specialists' Meeting on Aerodynamics and Aeroacoustics, Feb. 25–27, 1987.

8. Totah, J.: A Critical Assessment of UH-60 Main Rotor Blade Airfoil Data. 11th AIAA Applied Aerodynamics Conference, Aug. 1993.

9. Hooper, W.: The Vibratory Loading of Helicopter Rotors. Vertica, vol. 8, 1984. Also: Ninth European Rotorcraft Forum, Sept. 1983.

10. Bousman, W.: The Response of Helicopter Rotors to Vibratory Airloads. Journal of the American Helicopter Society, vol. 34, no. 4, Oct. 1990.

REPORT DOCUMENTATION PAGE

Form Approved
OMB No. 0704-0188

1. AGENCY USE ONLY *(Leave blank)*	2. REPORT DATE	3. REPORT TYPE AND DATES COVERED
	August 1996	Technical Memorandum

4. TITLE AND SUBTITLE

Aerodynamic Limitations of the UH-60A Rotor

5. FUNDING NUMBERS

505-59-36

6. AUTHOR(S)

Colin P. Coleman and William G. Bousman*

7. PERFORMING ORGANIZATION NAME(S) AND ADDRESS(ES)

Ames Research Center, Moffett Field, CA 94035-1000 and
Aeroflightdynamics Directorate, U.S. Army Aviation and Troop Command, Ames Research Center, Moffett Field, CA 94035-1000

8. PERFORMING ORGANIZATION REPORT NUMBER

A-961611

9. SPONSORING/MONITORING AGENCY NAME(S) AND ADDRESS(ES)

National Aeronautics and Space Administration
Washington, DC 20546-0001 and U.S. Army Aviation and Troop Command, St. Louis, MO 63120-1798

10. SPONSORING/MONITORING AGENCY REPORT NUMBER

NASA TM-110396
USAATCOM TR-96-A-011

11. SUPPLEMENTARY NOTES

Point of Contact: Colin P. Coleman, Ames Research Center, MS 260-1, Moffett Field, CA 94035-1000
(415) 604-0613
*Aeroflightdynamics Directorate, U.S. Army Aviation and Troop Command, Moffett Field, California.

12a. DISTRIBUTION/AVAILABILITY STATEMENT

Unclassified — Unlimited

Subject Category – 02

12b. DISTRIBUTION CODE

13. ABSTRACT ***(Maximum 200 words)***

High quality airloads data have been obtained on an instrumented UH-60A in flight and these data provide insight into the aerodynamic limiting behavior of the rotor. At moderate weight coefficients and high advance ratio limiting performance is largely caused by high drag near the blade tip on the advancing side of the rotor as supercritical flow develops on the rotor with moderate to strong shocks on both surfaces of the blade. Drag divergence data from two-dimensional airfoil tests show good agreement with the development of the supercritical flow regions. Large aerodynamic pitching moments are observed at high advance ratio, as well, and these pitching moments are the source of high torsional moments on the blade and control system loads. These loads occur on the advancing side of the disk and are not related to blade stall which does not occur for these weight coefficients. At high weight coefficients aerodynamic and structural limits are related to dynamic stall cycles that begin on the retreating side of the blade and, for the most severe conditions, carry around to the advancing side of the blade at the presumed first frequency of the blade/control system.

14. SUBJECT TERMS	15. NUMBER OF PAGES
UH-60, Aerodynamic, Flight test	18
	16. PRICE CODE: A03

17. SECURITY CLASSIFICATION OF REPORT	18. SECURITY CLASSIFICATION OF THIS PAGE	19. SECURITY CLASSIFICATION OF ABSTRACT	20. LIMITATION OF ABSTRACT
Unclassified	Unclassified		